Weld Microstructure Development and Properties of Precipitation-Strengthened Martensitic Stainless Steels

The cracking behavior and mechanical properties are discussed in terms of microstructural evolution

BY J. A. BROOKS AND W. M. GARRISON, Jr.

ABSTRACT. The weld microstructural evolution, mechanical properties and solidification cracking susceptibility of three precipitation-strengthened martensitic stainless steels — PH 13-8 Mo, Custom 450 and 15-5 PH — were investigated. Liquid tin quenching of gas tungsten arc welds revealed that all three welds solidified as single-phase ferrite with a high degree of microsegregation. However, during further solidification and cooling almost complete homogenization occurred as a result of solid-state diffusion. The welds in all three alloys exhibited good resistance to solidification cracking and generally exhibited tensile and impact properties similar to those of the base metal. However, in almost all cases, the weld Charpy impact energies were somewhat less than those of the base metals. The cracking behavior and mechanical properties are discussed in terms of microstructural evolution.

Introduction

The precipitation-strengthened martensitic stainless steels are used for their high strength, higher than that of the austenitic stainless steels, and good corrosion resistance, better than the hardenable 400 series stainless steels (Ref. 1). These alloys form a low-carbon martensite with M_f temperatures just above room temperature, and are precipitation strengthened by one or more of the following elements: Cu, Al, Ti, Nb and Mo (Refs. 2–4). In general, these materials exhibit good weldability; however, they exhibit an embrittlement coincident with the onset of precipitation hardening that has precluded the use of some alloys of this type in applications requiring high toughness (Ref. 5).

Often, the evolution of the weld microstructure is not well understood or considered by the welding engineer or metallurgist. Rather, emphasis is directed at developing a defect-free weld that meets minimum property requirements. Although the engineering application is of primary importance, only by understanding the evolution of the microstructure can one expect to readily optimize welding processes and subsequent weld properties. The evolution of weld microstructures of these alloys has never been studied in detail. This investigation studies three such alloys: PH 13-8 Mo (USN S13800), strengthened by NiAl; 15-5 PH (USN S15500), strengthened by particles of elemental Cu; and Custom 450 (USN S45000), strengthened with particles of elemental Cu and possibly a Nb- and Mo-containing Laves phase. The solidification cracking susceptibility and weld tensile and impact properties were investigated and are discussed in terms of microstructural evolution revealed with the use of liquid tin quenching.

KEY WORDS

Austenite
Charpy Impact Energy
Ferrite
Microstructure
Precipitation Hardening
Solidification
Tin Quenching
Varestraint Testing

J. A. BROOKS is with Sandia National Laboratories, Livermore, Calif. W. R. GARRISON, Jr., is with Carnegie-Mellon University, Pittsburgh, Pa.

Experimental

Compositions of the three martensitic stainless steels are shown in Table 1. All three alloys were from commercial heats. The VAR PH 13-8 was obtained from Armco and the ESR Custom 450 was obtained from Carpenter Technology. Both alloys were in the form of an 8-in. round corner square bar. The 15-5 PH was obtained from G. O. Carlson in the form of ½-in. plate. The PH 13-8 and Custom 450 were upset and cross forged at 1200°C (2192°F) to plate 0.6 and 0.4 in. thick, 14 in. wide and approximately 3 ft long. Smooth axisymmetric tensile properties and the Charpy impact energy were determined for both welds and base metals in the unaged condition and as a function of aging temperature. The mechanical properties of the base plates were obtained using specimens that were austenitized, oil quenched and then aged. Refrigeration to liquid nitrogen temperature subsequent to oil quenching and prior to aging had negligible effects on the strength and Charpy impact properties of Custom 450 and 15-5 PH when aged between 450 and 550°C (842–1022°F) for 1 h. Under the same conditions, the impact toughness of PH 13-8 was actually reduced ~20% when aged at 450°C and reduced ~30% when aged at 500°C, while the yield strength increased ~3 and 6%, respectively, as a result of refrigeration. When aged at 550°C, the properties were unaffected as a result of refrigeration prior to aging. Consequently, refrigeration was not used on any of the specimens in this study. Weld plates 6.4 x 30.5 cm (2.5 x 12 in.) were austenitized for 1 h and air cooled prior to welding. An austenitizing temperature of 927°C (1700°F) was used for PH 13-8 Mo while that for Custom 450 and 15-5 PH was 1038°C (1900°F).

Mechanical test specimens were cut from GTA cold wire feed welds with the

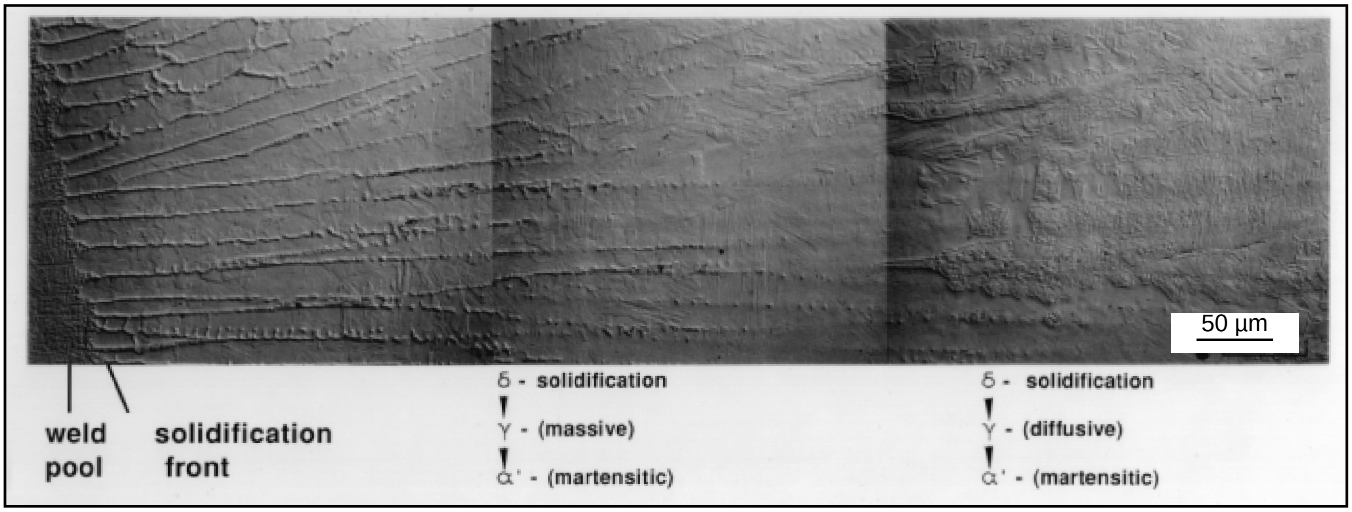

Fig. 1 — Montage of liquid tin-quenched Custom 450 GTA weld showing the evolution of the weld microstructure from the dendrite tips in the weld pool to the region of solid-state transformation of ferrite to austenite. Captions show sequence of transformations.

Table 1 — Alloy Compositions (wt-%)

Alloy	C	Cr	Ni	Cu	Al	Mo	Si	Mn	Nb	P	S	N
PH 13-8 Mo	0.03	12.63	7.9	—	1.08	1.73	0.04	0.05	—	0.005	0.005	0.002
Custom 450	0.03	14.75	6.44	1.5	—	0.76	0.4	0.33	0.75	0.008	0.005	0.035
15-5 PH	0.02	14.7	4.7	3.2	—	0.38	0.33	0.33	0.2	0.017	0.007	—
304L-F	0.017	19.1	10.7	—	—	0.21	0.54	1.9	—	0.24	0.001	0.035
304L-A	0.020	18.7	10.9	—	—	0.19	0.53	1.7	—	0.020	0.008	0.035

sample length transverse to the weld direction. The weld fusion zone was placed in the center of the specimens with the notch of the Charpy specimens at the weld root. Tensile specimens, 5 mm in diameter and 20 mm long (0.2 x 0.79 in.), contained a composite of the fusion zone (~50%), HAZ and base metal. The tensile specimens deformed uniformly when tested, indicating no one zone dominated the tensile response; specimens also fractured near the weld center. The nominal weld parameters and plate thicknesses corresponding to the test results are shown in Table 2. A U-groove joint preparation and 1.14-mm (0.045-in.) welding wire were used with an interpass temperature of ~65°C (~150°F) for both plate thicknesses.

Table 2 — Nominal Weld Parameters

Samples	Thickness (in.)	Amps	Volts	Speed (in./min.)	Wire Feed (in./min.)	No. Passes
Varestraint	0.25	180	12	6.0	—	1
Tensile	0.375	200	10	6.0	20	14–16
Charpy	0.5	200	10	6.0	20	20–24

The solidification cracking susceptibility was evaluated in the unaged condition using sub-size Varestraint testing (Ref. 6). For comparison, tests were conducted on two commercial vacuum-induction melted/vacuum-arc remelted heats of 304L (USN S30403): one that solidified as primary ferrite, designated 304L-F, and the other that solidified as primary austenite, designated 304L-A. The compositions of these two heats of 304L are shown in Table 1. Welding parameters used during Varestraint testing are given in Table 2.

Metallographic samples of tin quenched and Varestraint specimens were prepared using standard metallographic techniques with the final polish made with a 0.05-micron silica aqueous solution. A Vilella's etch was used to reveal the microstructural features. Microprobe analysis for compositional determination was conducted using a Joel 8900 microprobe with a 1-micron beam size operated at 15 and 25 KEV, depending upon feature size, and a 25-nA beam current. Samples for TEM analysis were electropolished and examined on a Joel 200 CX microscope. Fracture surfaces of Charpy samples were examined using SEM.

Microstructural Evolution

In this investigation, GTA welds were quenched with liquid tin during welding in an attempt to capture insitu the evolution of the weld microstructure from the first stages of solidification to that observed at room temperature. Figure 1 shows results from a Custom 450 weld obtained using this technique. The microstructure is evolving from left to right with the quenched weld pool and solidifying dendrite tips shown in the left side of the micrograph. Microsegregation occurring from elemental partitioning between the solid and liquid during weld solidification is evident in the interdendritic regions of the cellular/cellular-dendritic solidifying structure. However, it appears that homogenization occurs during further solidification and cooling (moving from left to right in the micrograph). At a lower temperature (in the right-hand side of the micrograph), the ferrite has started to transform to austenite by a diffusion-controlled process. When cooled below the M_s (in this case, assisted by the tin quenching), the austenite transforms to martensite. Thus, the total evolution of the weld microstructure can be observed in one micrograph.

Electron microprobe analysis was

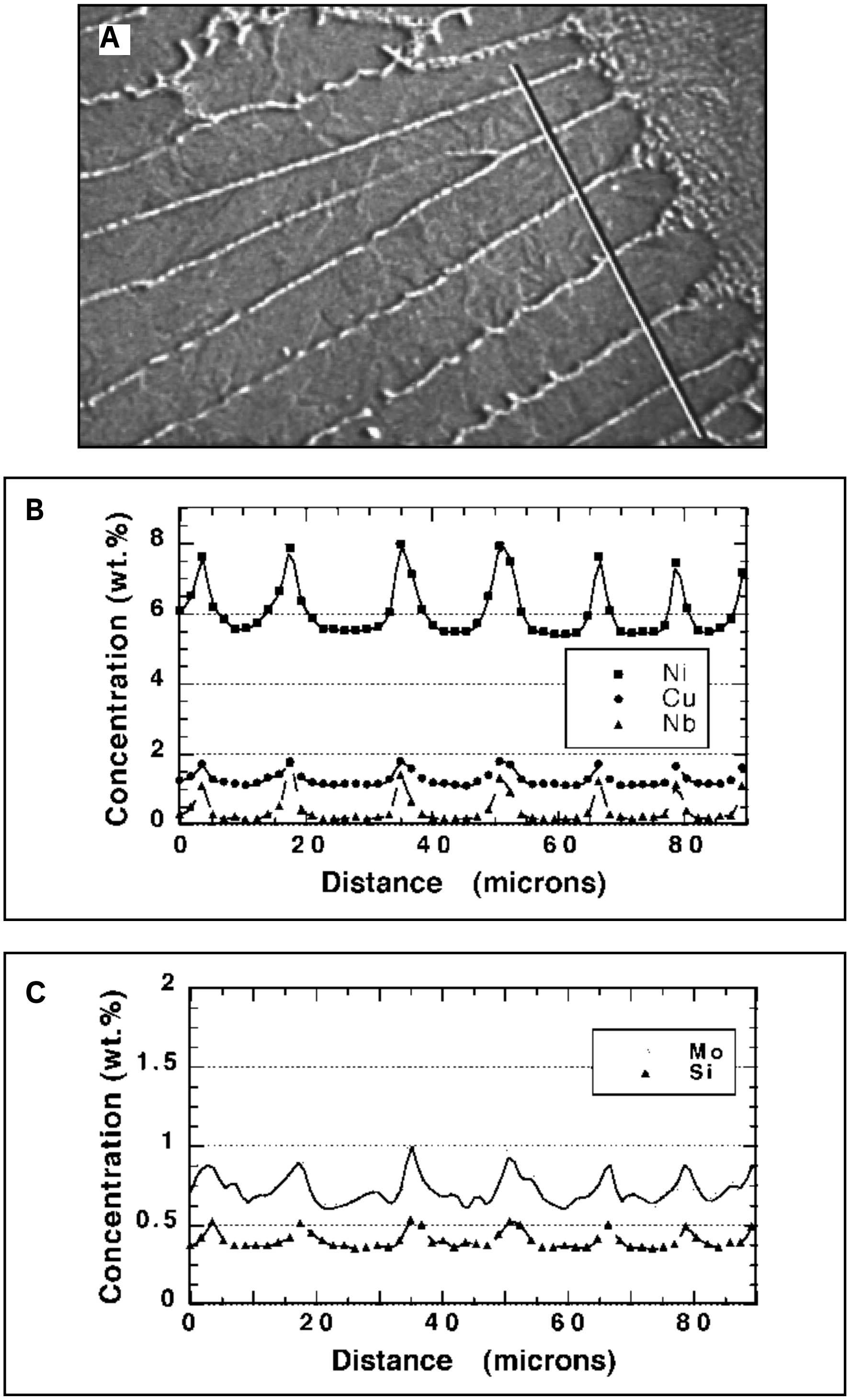

Fig. 2 — SEM micrograph (A) showing solidification front of sample in Fig. 1. The line indicates region of microprobe analysis shown in B and C.

Table 3 — Measured Initial Partitioning Coefficients

Element	Ni	Mo	Nb	Cu	Si
Custom 450	0.85	0.82	0.36	0.9	0.88
PH 13-8 Mo	0.88	0.84	—	—	—

conducted to determine elemental partitioning and microsegregation in the quenched Custom 450 weld sample shown in Fig. 1. An analysis using a 1.75-micron spacing was taken across the dendritic structure near the solidification front in the region shown at higher magnification — Fig. 2A. The results are shown for Ni, Nb, Cu, Mo and Si in Fig. 2B, C. It can be seen the partitioning coefficients (k defined as C_s/C_l, where C_s = concentration of the solid and C_l = concentration in liquid) are less than 1 for all these elements. That is, the intracellular regions, the first to solidify, are depleted in these elements and the cell boundaries, the last regions to solidify, are enriched. Partitioning coefficients near the liquidus, calculated using microprobe analysis of the cell tips and the bulk composition given in Table 1, are shown in Table 3. Although carbon was not measured, it is known that carbon also partitions to the liquid, k<1.

The interdendritic region near the solidification front is shown at higher magnification in the SEM micrograph of Fig. 3. As discussed below in the section on solidification cracking, the second phase is composed primarily of NbC. It is important to note in the optical micrograph of Fig. 1 that, at a distance of about 400 microns (0.016 in.) from the solidification front, little evidence of the second phase exists.

An electron microprobe analysis, again using a spacing of 1.75 microns (6.9 x 10^{-5} in.), was conducted transverse to the weld along a line 400 microns from the weld front where in Fig. 1 there is no evidence of microsegregation. The microprobe analysis shown in Fig. 4 for Ni, Nb and Cu verified the material in this region is very homogeneous compared to the region near the solidification front shown in Fig. 2A. The Ni variation was reduced from ~2.5 wt-% at the solidification front to only ~0.7 wt-% at a distance 400 microns from the solidification front. Similarly, variations were reduced in Cu from 0.65 to 0.2 wt-%, in Nb from 1.2 to 0.2 wt-%, in Si from 0.35 to 0.04 wt-% and in Mo from 0.4 to 0.1 wt-%.

Welds of PH 13-8 were also liquid tin quenched. This alloy solidified in the same fashion as Custom 450, that is, as single-phase ferrite. The microstructures in Fig. 5A taken near the solidification front clearly show evidence of alloy partitioning that occurred during weld solidification. Microprobe analysis was conducted in regions of the cell core and cell boundaries. The average of a number of analyses in the two regions were the following: Ni core = 7.6 wt-%, boundary =10.5 wt-%; Mo core = 1.9 wt-%,

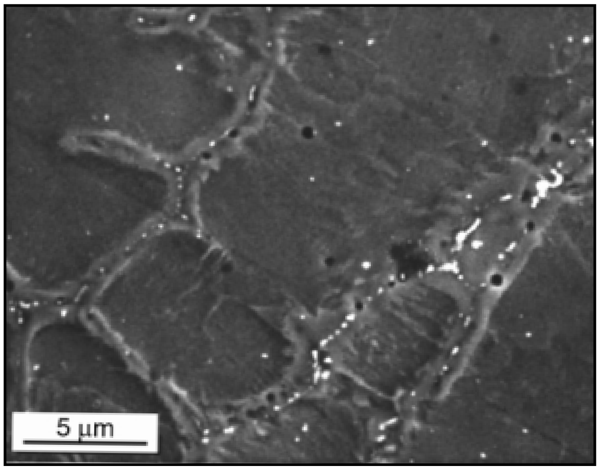

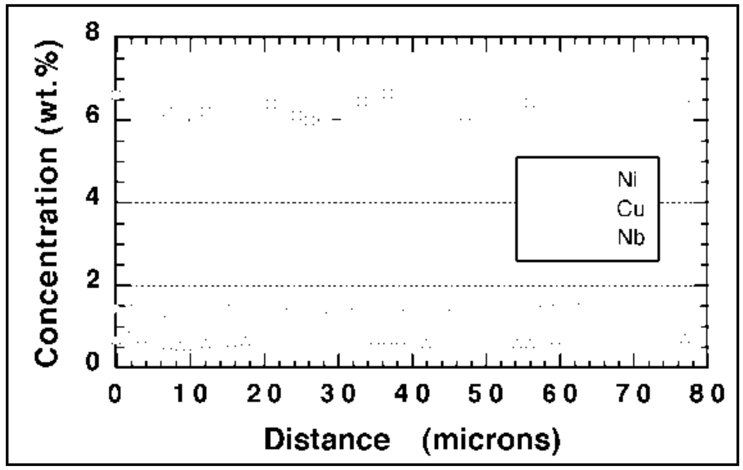

Fig. 3 — SEM micrograph showing at higher magnification the dendritic region near the tin-quenched solidification front of the Custom 450 weld.

Fig. 4 — Microprobe analysis taken across the dendrite structure ~400 microns from the solidification front of the sample shown in Fig. 1.

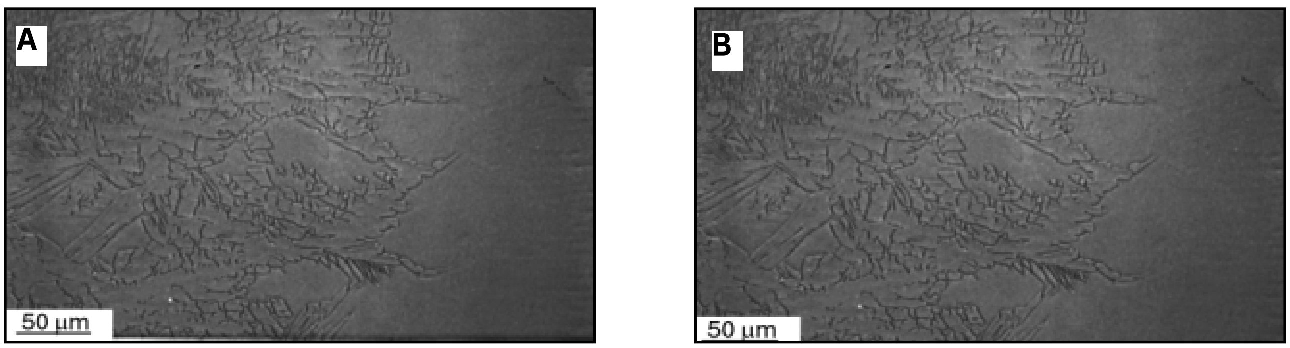

Fig. 5 — A — Solidification structure near the weld pool (to the right) of a liquid tin-quenched PH 13-8 Mo GTA weld showing evidence of alloy segregation; B — region of the decomposition of ferrite to austenite ~1 mm from the solidification front.

boundary = 2.6 wt-%; and Al core = 1.2 wt-% and boundary = 1.4 wt-%. However, it can be seen in this sample the very tips of the solidifying dendrites have not been captured. Thus, it must be expected that, as a result of some solid-state diffusion occurring during solidification, the concentrations measured at the dendrite cores are somewhat higher than what would exist at the dendrite tips. Therefore, the initial partitioning coefficients shown for PH 13-8 in Table 3 are likely somewhat high.

The region of the solid-state transformation of ferrite to austenite is shown in Fig. 5B ~1000 microns (~0.039 in.) from the weld front. Note that in the region of the quenched ferrite no evidence of segregation exists. Similar to Custom 450, homogenization of the PH 13-8 welds also occurred during solidification and cooling. As a result of elemental partitioning during the ferrite-to-austenite transformation, a small amount of ferrite is retained along the Widmanstatten austenite boundaries. In this weld, the ferrite fraction appeared to be 1–2%.

Discussion of Microstructure Evolution

In Custom 450, as well as the other two alloys studied, little evidence of microsegregation exists in the room-temperature weld microstructures. Thus, one may have expected that partitioning coefficients could be close to 1. However, in the tin-quenched samples it was found a high degree of alloy partitioning does occur during solidification. The experimentally measured partitioning coefficients shown in Table 3 vary from ~0.85 for Ni to ~0.36 for Nb. It is evident during solidification and cooling, even at the fairly rapid cooling rates of welding, a large degree of homogenization can occur. This observed behavior is in agreement with the weld solidification model developed by Brooks and Baskes (Ref. 7) in which they incorporated solid-state diffusion. In their models, they showed, for example, that Nb in Fe, with a partitioning coefficient of ~0.25, rapidly diffuses during weld solidification, resulting in a nearly homogeneous composition. However, more recently they have shown that even in GTA welds undercooling can result in higher Nb concentrations of the dendrite tip, but this effect is diminished during further solidification and cooling as a result of solid-state diffusion (Ref. 8). It must be expected that, in the welds in this study, some tip undercooling also occurred that slightly increased the initial dendrite tip concentration above the equilibrium value for elements with partitioning coefficients less than 1.

The quenching results shown for Custom 450 and PH 13-8 provide insight to the microstructural evolution of other martensitic stainless steels. In both Custom 450 and PH 13-8, the welds solidified as single-phase ferrite with no secondary solidification of austenite. One can predict the solidification behavior of stainless steels using Cr_{eq}/Ni_{eq} ratios (Ref. 9) from a variety of diagrams, such as the WRC-1992 diagram (Ref. 10). For the composition of Custom 450 used here, the Cr_{eq}/Ni_{eq} ratio, using the WRC, is 1.87, above the minimum value of ~1.7 predicting solidification occurring com-

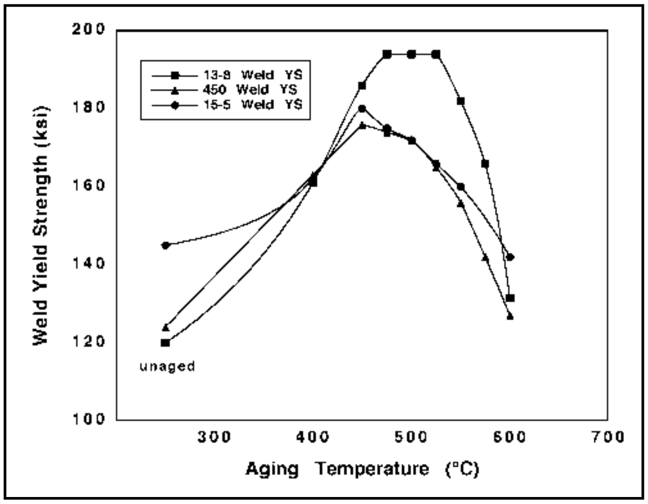

Fig. 6 — Transverse weld tensile yield strengths (0.2% offset) of the three alloys studied.

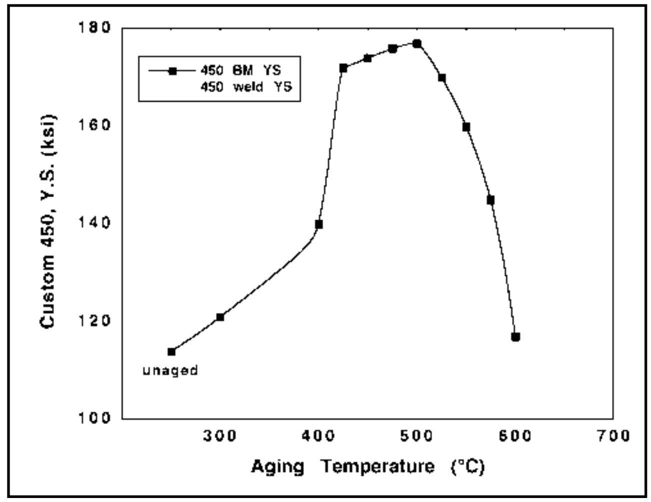

Fig. 7 — Yield strengths of weld and base metals of Custom 450 in the unaged condition and as a function of aging temperature.

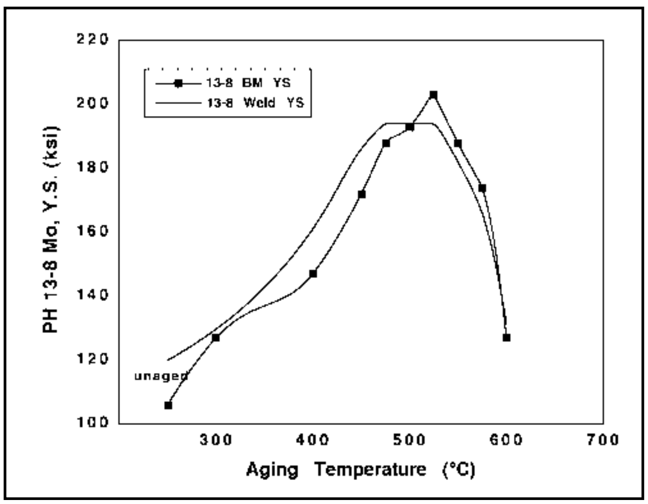

Fig. 8 — Yield strengths of weld and base metals of PH 13-8 Mo in the unaged condition and as a function of aging temperature.

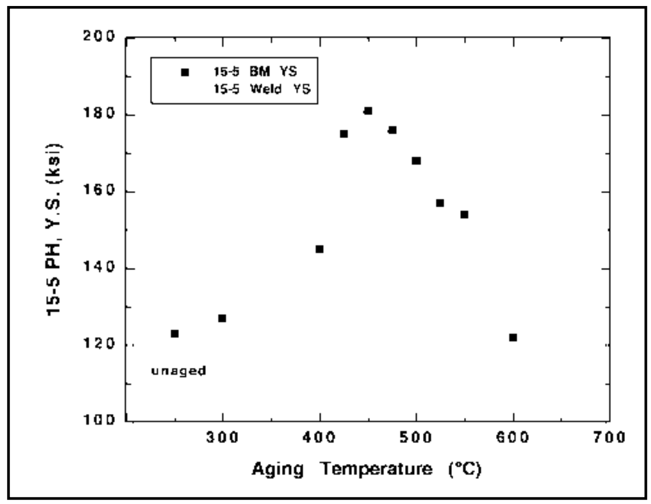

Fig. 9 — Yield strengths of weld and base metals of 15-5 PH in the unaged condition and as a function of aging temperature.

pletely as ferrite. This prediction of ferrite solidification is consistent with the behavior shown in Fig. 1. The Cr_{eq}/Ni_{eq} ratio for 15-5 PH (using N=0.03) and PH 13-8 are 2.24 and 1.60, respectively. One would then predict that 15-5 PH would also solidify as single-phase ferrite and exhibit similar behavior to that shown in Fig. 1. However, it may have been expected that the heat of PH 13-8 with a Cr_{eq}/Ni_{eq} ratio of 1.60 used in this study would have solidified as primary ferrite with the peritectic solidification of austenite. The tin-quenched welds of the PH 13-8 alloy clearly showed that solidification occurred as single-phase ferrite, with the solid-state transformation taking place at a temperature considerably lower than that of final solidification. However, as discussed by Cieslak, *et al.* (Ref. 11), if Al is included in the Cr_{eq} with a value of 2.48, the Cr_{eq}/Ni_{eq} is 1.90, well within the single-phase ferrite solidification region.

It is interesting to note in Fig. 1 a martensitic structure is evident throughout the microstructure. In the lower temperature regions of the micrograph (right side), the ferrite that transformed via a diffusional process to austenite transformed to martensite when cooled to a little above room temperature, M_s~120°C (250°F). The microstructure in the left side of the micrograph is different than that on the right side. It is proposed that, at the higher temperatures near the weld front, rapid cooling rates during quenching suppressed the diffusion-controlled transformation of ferrite to austenite, allowing the ferrite to transform massively (Ref. 12) to austenite, as has been reported in some austenitic stainless steels (Refs. 13, 14). It has also been suggested a massive transformation can occur during water quenching thin sheets of PH 13-8 (Ref. 13). Upon further cooling, this austenite also transformed to martensite. This later sequence of transformations is a manifestation of the tin quench and is not representative of the microstructural evolution of the GTA welds. However, this sequence of transformations could occur under the rapid cooling rates of the high-energy-density welding processes.

Mechanical Properties

The tensile properties of both welds and base metal were obtained for the unaged condition and as a function of aging temperature for an aging time of 3.2 h. An aging time of 3.2 h was chosen for direct comparisons with base metal

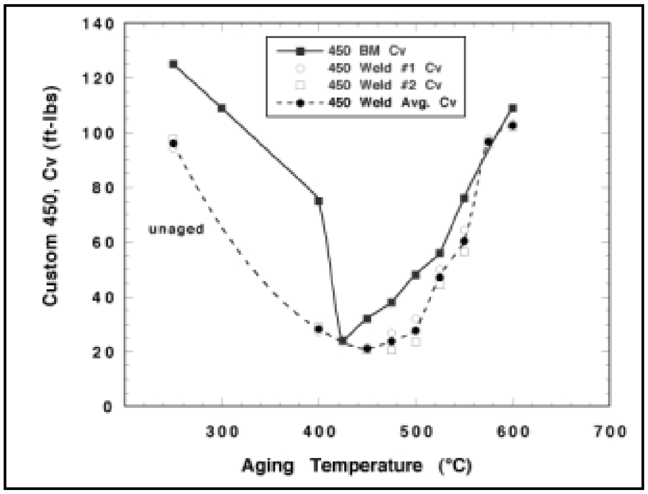

Fig. 10 — Charpy impact energies of the weld and base metals for Custom 450 in the unaged condition and as a function of aging temperature.

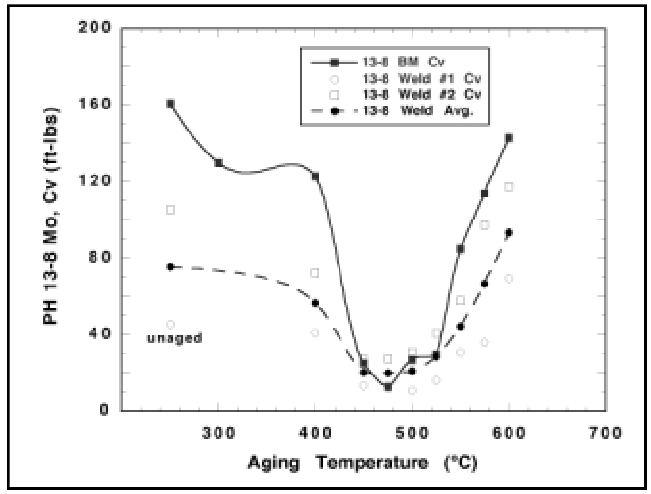

Fig. 11 — Charpy impact energies of the weld and base metals for PH 13-8 Mo in the unaged condition and as a function of aging temperature.

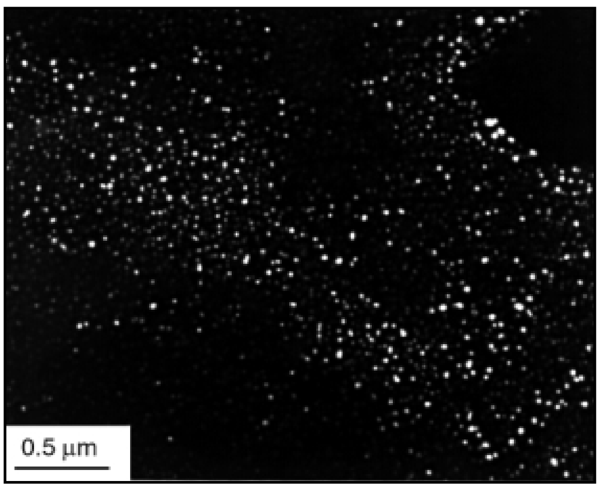

Fig. 12 — TEM dark field micrograph of PH 13-8 Mo weld fusion zone aged for 3.2 h at 550°C showing distribution of NiAl.

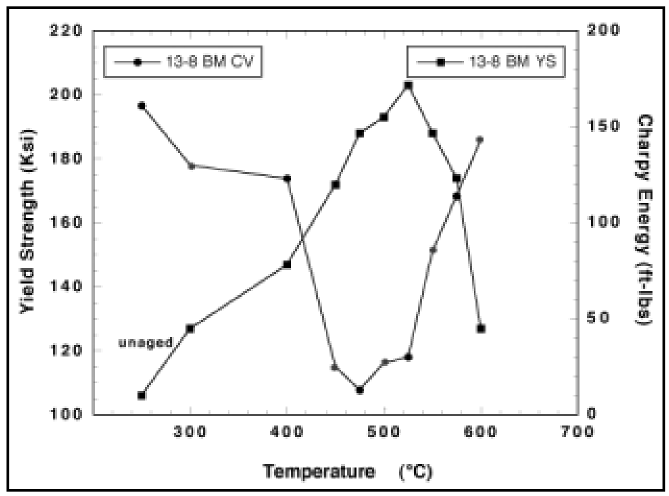

Fig. 13 — Charpy impact energy and yield strength of PH 13-8 Mo base metal plotted as a function of aging temperature.

properties for which aging times of up to 100 h were studied (1, 3.2, 10, 32 and 100 h). The 3.2 h is close to the conventional aging time of 4 h for these materials. The tensile data reported are the averages of two tests in which the variation in the two test results were typically within several ksi for both the welds and base metals. The weld tensile yield strengths are shown in Fig. 6. The aging response of the welds of all alloys is similar in that the yield strength reaches a maximum at intermediate aging temperatures and then decreases with further increases in aging temperature. Peak yield strengths for the 3.2-h age were about 195 ksi for PH 13-8 and about 180 ksi for Custom 450 and 15-5 PH. The peak strengths of Custom 450 and 15-5 PH are reached at an aging temperature 50–75°C less than the aging temperature at which the peak yield strength was achieved for PH 13-8, ~450 vs. 525°C (842 vs. 977°F).

The yield strengths of the weld and base metal of the three alloys studied are plotted in Figs. 7–9 as a function of aging temperature. In all the alloys, the nature of the aging response is similar, though varying slightly in detail. Therefore, their general behavior can be discussed together. In the unaged condition, the welds have a higher yield strength than the base metals. This trend also exists for the lower aging temperatures, with the peak strengths of the welds and base metals being very similar. Except for 15-5 PH, the peak strength of the welds is reached at an aging temperature ~50°C lower than that of the base metals. For aging temperatures greater than that producing peak strength, the base metal of both Custom 450 and PH 13-8 has slightly higher strengths than the weld metal. However, in all three alloy systems the welds have a higher strength than the base metal when aged at 600°C (1112°F). Thus, the results suggest that weld microstructures age harden more intensely at lower aging temperatures and the weld microstructures overage more slowly than the base metals.

The Charpy impact energies of Custom 450 and PH 13-8 welds and base metals were determined for the unaged conditions and as a function of aging temperature for an aging time of 3.2 h. As shown in Fig. 10, the Charpy impact energy of the Custom 450 base metal is

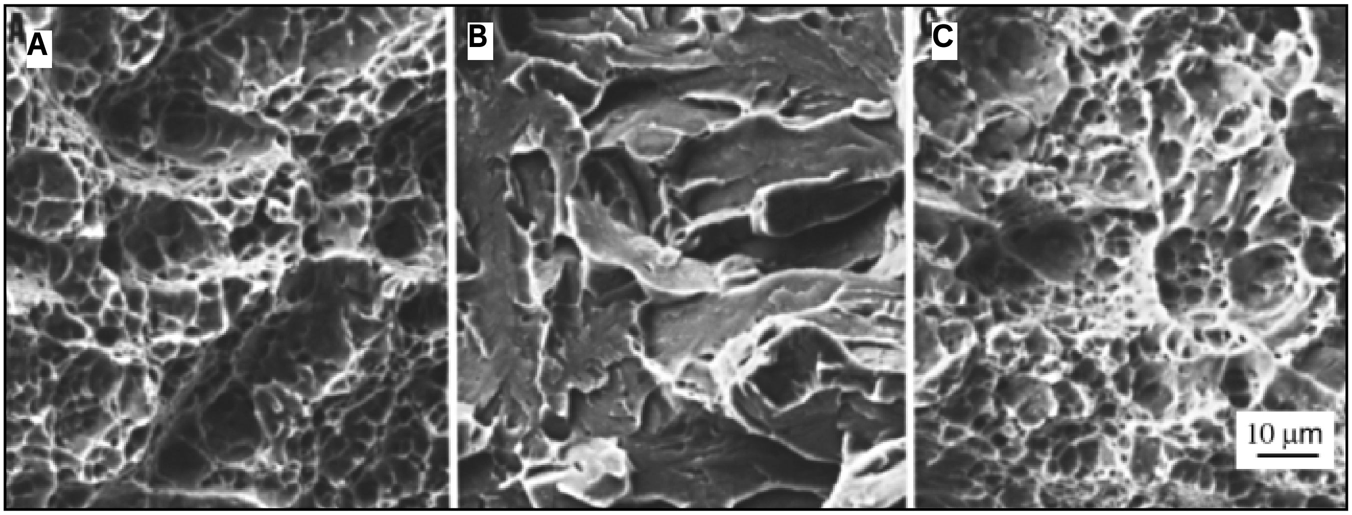

Fig. 14 — Fracture surfaces of Charpy impact specimens of PH 13-8 Mo base metal aged at: A — 450°C; B — 500°C; C — 550°C (all same magnification).

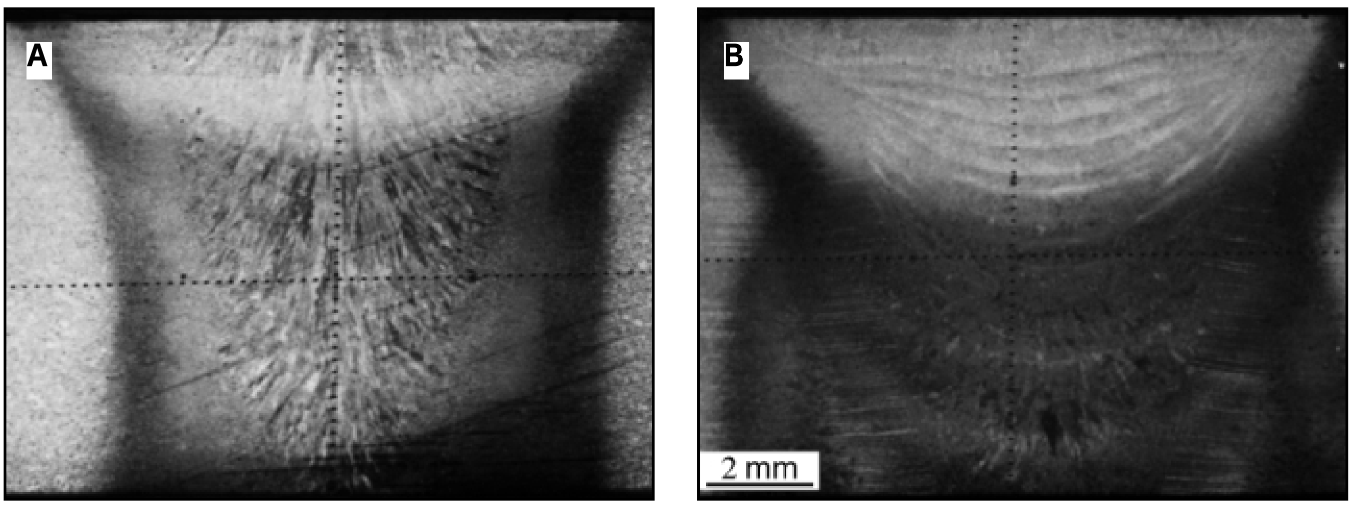

Fig. 15 — Cross sections of the welds of: A — Custom 450; B — PH 13-8 Mo.

125 ft-lb in the unaged condition and decreases with increasing aging temperature to a minimum value of 24 ft-lb on aging at 425°C (797°F). On aging above 425°C, the impact energy increases with increasing aging temperature. The Charpy impact energies obtained from the two weld plates of Custom 450 are quite similar, as shown in Fig. 10. In the unaged condition, they are ~25% lower that that of the base metal. At an aging temperature of 400°C (752°F), the impact energy drops drastically to only ~35–40% of that of the base metal. At aging temperatures from 450 to 550°C (842 to 1022°F), the Charpy impact energy of the weld metal is still less than that of the base metal, even though in this range the Charpy impact energy of both the weld and base metal increase with increasing aging temperature.

The Charpy impact energies of the weld and base metals for PH 13-8 are shown in Fig. 11. In the unaged condition, the impact energy of the base metal is quite high, at 161 ft-lb, but decreases to 25 ft-lb at aging temperatures between 450 and 525°C. For aging temperatures greater than 525°C, the Charpy impact energy increases rapidly with increasing aging temperature. Thus, for the base metal, there is an embrittlement of the alloy that coincides with the onset of significant age hardening, and the minimum in Charpy impact energy is obtained at an aging temperature about 50°C lower than the aging temperature at which the maximum yield strength is obtained. Both welds exhibit behavior qualitatively similar to that of the base metal, but the levels of toughness achieved by the two welds are very different. Weld 2 has a Charpy impact energy in the unaged condition of 105 ft-lb, while the Charpy impact energy of weld 1 in the unaged condition is only 56 ft-lb. While both welds exhibit an embrittlement trough in the same range of aging temperatures as exhibited by the base metal, material from Weld 1 is, at every aging temperature, of lower toughness than material taken from Weld 2.

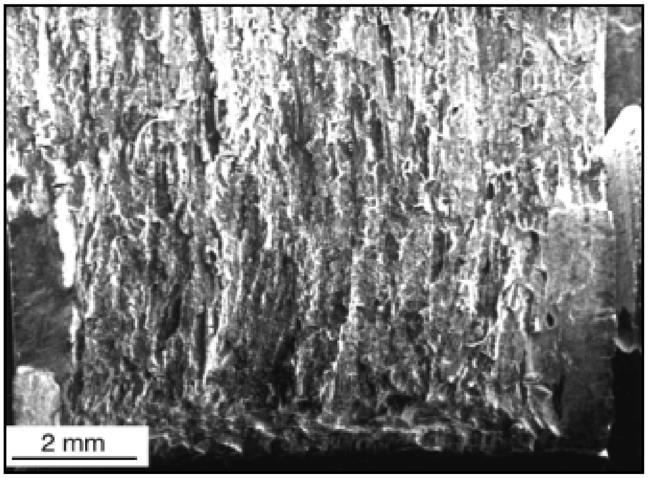

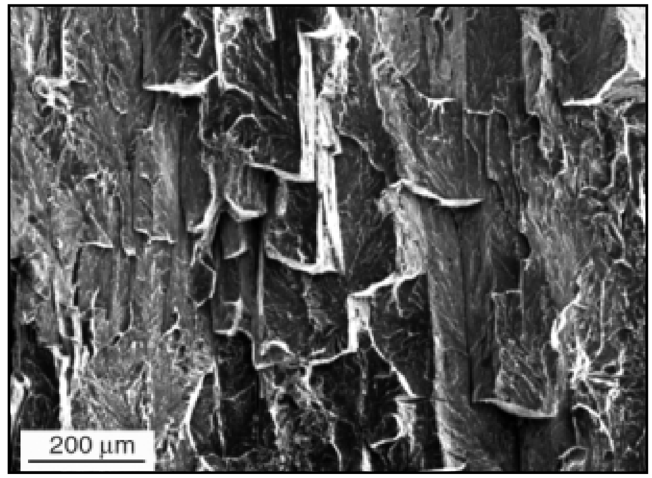

Fig. 16 — Fracture surfaces at two magnifications of Custom 450 weld Charpy impact specimen aged at 475°C. The fracture path is bottom to top in both fractographs.

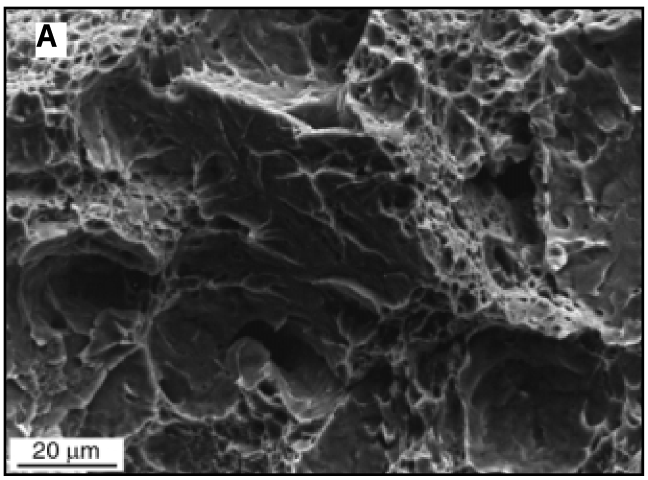

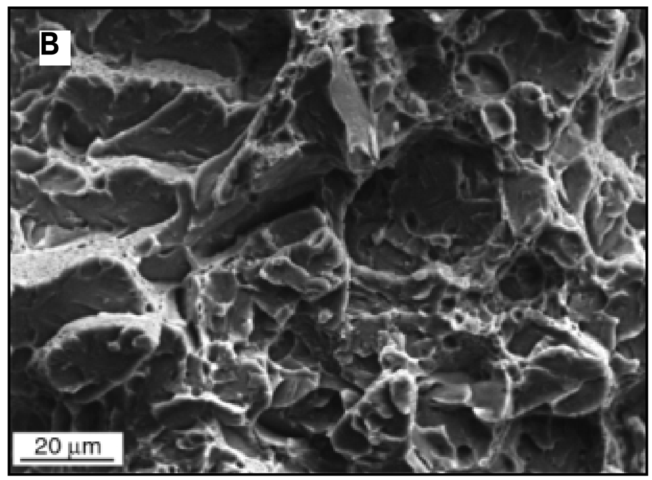

Fig. 17 — Fracture surfaces of Custom 450 base metal Charpy impact specimens: A — Aged at 475°C for 3.2 h; B — aged at 450°C for 100 h.

Discussion of Mechanical Properties

In using these materials, one must choose the aging temperature that provides the best combination of strength and toughness for the particular engineering application. The differences in weld and base metal aging response must then also be considered. Qualitatively, for a given alloy type, the base metals and welds exhibited similar age-hardening responses in that similar peak yield strengths were obtained and the peak yield strengths were obtained at similar aging temperatures. However, there are consistent differences.

The primary difference between the base and weld metal aging responses was that the weld metals exhibited higher strengths than did the base metals in the unaged condition and at the lower aging temperatures. This effect is believed to be due to the thermal cycles experienced by weld deposits from subsequent weld passes. After each weld pass, the weld plates were allowed to cool to below about 65°C, less than the martensite start temperatures for PH 13-8, Custom 450 and 15-5 PH, which are 120, 118 and 132°C (248, 244 and 270°F), respectively. Therefore, one would expect a new weld pass to have the effect of heating some region of the previously deposited weld to temperatures sufficient to result in particle precipitation in the martensite. While the times at these temperatures may be relatively brief and the temperature excursions themselves may not result in marked age hardening of the martensite, they could have the effect of altering particle precipitation kinetics on subsequent aging of the weld. This is consistent with the yield strengths of the welds being greater than the yield strengths of the base metals in the unaged conditions, the welds having higher yield strengths than the base metals after aging at 400°C (752°F) and the weld metals achieving their maximum yield strength at lower aging temperatures than those of the base metals.

While there were small but consistent differences between the aging responses of weld and base metals for these alloys, the peak strengths obtained for the base and weld metals after age hardening were similar. This similarity in strength can be related to the evolution of the weld microstructure, as observed in the tin-quenched samples. Here, it was shown that considerable alloy partitioning occurred during weld solidification, but solid-state diffusion was sufficiently fast for a large degree of homogenization

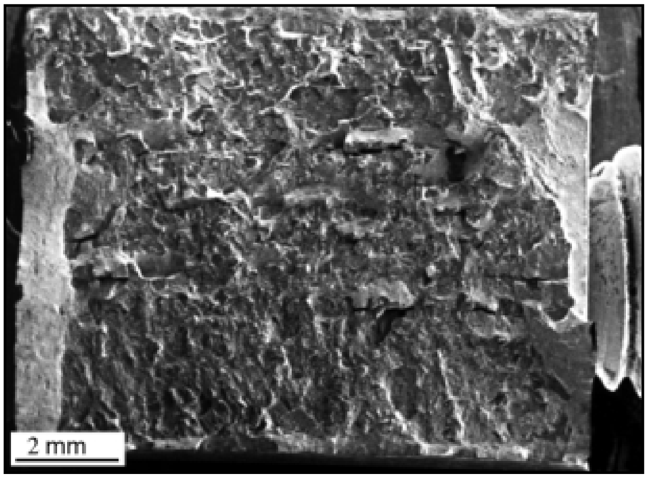

Fig. 18 — Fracture surface of PH 13-8 weld aged at 525°C. Note secondary cracking associated with weld filler passes.

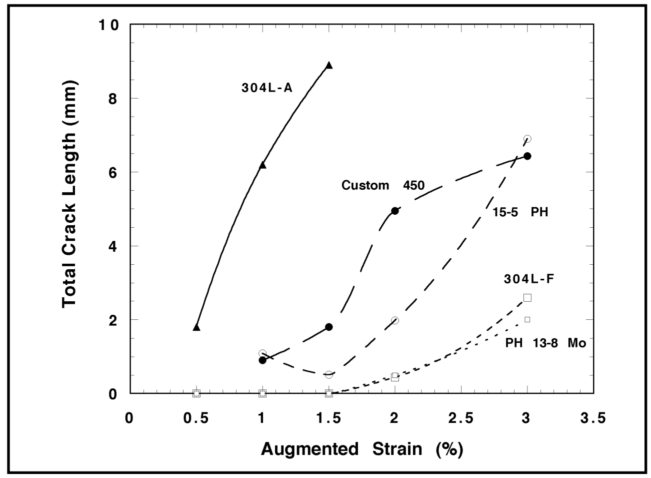

Fig. 19 — Subsize Varestraint test results showing solidification cracking behavior of the three martensitic stainless steels and two heats of 304L: 304L-A, primary austenite solidified, and 304L-F, primary ferrite solidified.

to occur during further solidification and cooling. This resulted in a uniform precipitate distribution throughout the weld microstructure represented in the TEM micrograph (Fig. 12) taken from the fusion zone of a PH 13-8 weld aged at 550°C (1022°F) for 3.2 h.

This behavior can be contrasted to the precipitation-strengthened austenitic stainless steels in which the high degree of microsegregation is retained to room temperature due to the sluggish diffusion kinetics in the austenitic structure. This often results in a nonuniform precipitate distribution with precipitate-free dendrite cores and welds with inferior mechanical properties (Refs. 15, 16). The similar aging response of the weld and base metal of the class of alloys studied here is an attractive engineering feature of these materials.

The Charpy impact energy results for the base and weld metal displayed similar behavior in that both exhibited a minimum in Charpy impact energy at an aging temperature slightly less than the aging temperature at which the peak yield strength was obtained. However, at most aging temperatures, the weld metal for both Custom 450 and PH 13-8 did not achieve the same levels of Charpy impact energy as did the base metals. There are also significant differences between the levels of toughness achieved by the two PH 13-8 weld plates. These differences in toughnesses can be discussed best by first reviewing the effect of aging temperature on the toughness of PH 13-8.

The Charpy impact energy and yield strength of PH 13-8 aged for 1 h are plotted as a function of aging temperature in Fig. 13. The room-temperature Charpy impact energy decreases dramatically on aging at 450°C, has a minimum on aging at 500°C (932°F) and then increases with increasing aging temperature. The minimum in Charpy impact energy occurs at an aging temperature 50°C less than that resulting in peak yield strength. The embrittlement of this alloy coincident with the onset of precipitation strengthening is associated with a change in fracture mode — Fig. 14. Even after aging at 450°C, fracture is by microvoid coalescence, but after aging at 500°C the fracture mode is primarily quasi-cleavage. As the aging temperature is increased beyond 500°C, the fracture mode returns to microvoid coalescence. It may be thought that this embrittlement behavior is related to microstructural changes associated with the decomposition of retained austenite, such as carbide precipitation at lath boundaries and/or changes in the mechanical stability of the retained austenite, or the precipitation of intra-lath particles. However, there is no evidence that in PH 13-8 there is any effect of aging temperature on austenite content, mechanical stability or morphology over the range of aging temperatures of interest (Ref. 5). It has also been found that in investment-cast material, austenite reversion does not occur at aging temperatures at or below 566°C (1051°F) (Ref. 18). Therefore, the embrittlement is ascribed to the precipitation of NiAl particles, which are coherent to the matrix and which would be expected to be sheared by dislocations at smaller particle sizes (Ref. 18). This shearing of particles is believed to result in a local work softening that promotes the strain localization required to initiate cleavage fracture.

The results for Custom 450 in Fig. 10 show that the Charpy impact energies in the unaged condition are less in the welds than in the base metal (~95 vs. 125 ft-lb). Three factors could be contributing to this difference in toughness. The first is that some precipitation of the strengthening particles is believed to have occurred in the weld metal; this alone would be expected to lead to reduced toughness in the weld metal. Second, the inclusion volume fraction and spacing in the weld metal could be different from those in the base metal. The particles in the base metal at which microvoids can initiate are primarily 5-micron-diameter Al- and Si-containing oxides, ~2-micron-diameter Nb-enriched carbonitrides and small ~0.15-micron Mn-enriched inclusions. By both introducing small amounts of oxygen and nitrogen during welding, which would increase the volume fraction of inclusions, and by refining particle size and spacing during weld solidification and cooling, the toughness would decrease (Refs. 19, 20). However, more work is needed to better characterize inclusions in weld deposits in these materials. The third factor that could result in lower weld metal toughness is the larger grain size, which can influence toughness when the fracture mode is microvoid coalescence and the inclusion spacing small, as in Custom 450 (Ref. 19).

The Custom 450 weld macrostructure, shown in cross section in Fig. 15, is characterized by a columnar grain structure that persists through the entire weld thickness. This structure is a result of epitaxial growth and preferred solidification growth directions. A low magnification fractograph of the Custom 450 weld aged

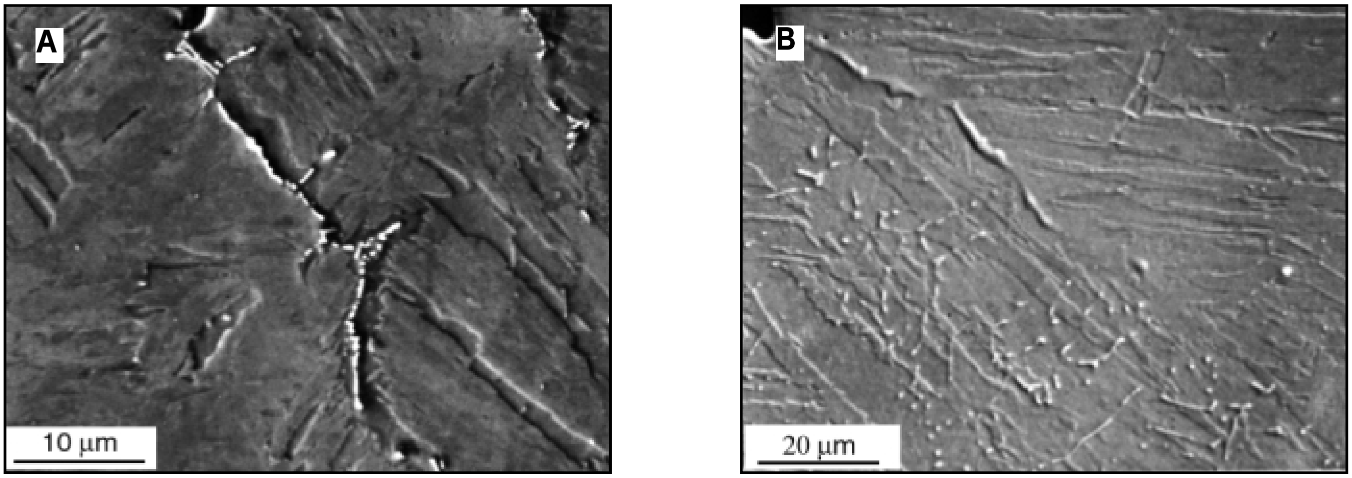

Fig. 20 — A — Solidification crack tips region of a Custom 450 Varestraint sample showing second phases associated with cracking (15-5 PH exhibited very similar appearance); B — solidification crack tip region of PH 13-8 Mo Varestraint sample.

at 475°C is shown in Fig. 16A. The fractograph indicates vertical striations associated with the long columnar grains observed in Fig. 15. This fracture surface is seen in higher magnification in Fig. 16B. These fractures exhibit a cleavage fracture mode with cleavage facets both parallel and perpendicular to the macroscopic fracture surface. The facets tend to have their longest dimension parallel to the columnar grains. If the cleavage facets are [100] planes, as is often observed in b.c.c. materials, the fractographs are consistent with the columnar grains having a [100] growth direction. For comparison, the fracture surface of Custom 450 base metal aged at 475°C (887°F) is shown in Fig. 17A. The fracture surface consists of both quasi-cleavage and microvoid coalescence, with cleavage facets 10–20 microns in dimension. The fracture surface of Custom 450 base metal aged at 450°C for 100 h, which resulted in a Charpy impact energy of about 8 ft-lb, is shown in Fig. 17B. The cleavage facets are more easily recognized on this fracture surface, but, again, they have dimensions of about 10 to 20 microns. Therefore, it is suggested that the lower toughness of the weld metal, particularly for aging temperatures of 450 through 500°C (842–1022°F) are strongly influenced by large and oriented grains, which promote cleavage fracture. However, after aging at 400°C (752°F), the strength of the weld metal is considerably greater than the strength of the base metal, as discussed previously. It is believed that the onset of the embrittlement at this temperature is primarily due to the precipitation of shearable particles.

In comparing the Charpy impact energies of the PH 13-8 weld and base metal, there are a number of points of interest. Again, the Charpy impact energies of the welds are less than the impact energy of the base metal for the unaged and aged (at 400°C) conditions. Microstructural factors that could lead to the weld metal having lower toughness than the base metal for the unaged condition and after aging at 400°C would be the same as those presented in the discussion of the toughness of Custom 450. However, it is not clear why one of the PH 13-8 welds had much higher toughness than the other, although it is believed to be due to microstructural differences introduced by welding. It is possible that there were slight undetected variations in the welding procedure between the two plates. The effects of different thermal cycles and interpass temperature of the multiple pass welds on the aging response, austenite reversion, carbide precipitation, etc., can be very complex in determining the final weld microstructure. More work is needed to determine the sensitivity of weld process variables on weld properties.

As shown in Fig. 14, the welds of PH 13-8 are not characterized by the long columnar grains observed for Custom 450. For PH 13-8, the regions associated with each weld pass appear to be clearly delineated and large columnar grains do not appear to continue past these boundaries, as they did in the Custom 450 welds. The interfaces between weld passes appear to be important to the fracture process. As shown in Fig. 18, the crack advancing from the base of the notch appears to interact strongly with these interfaces, and these interfaces are associated with secondary cracks — perpendicular to the fracture surface — exhibiting a ductile fracture mode. The energy absorbed by the secondary cracking processes could strongly influence the Charpy impact energy. These secondary cracks were not observed on the fracture surfaces of the Custom 450 welds that were examined. Given the high aluminum content of PH 13-8, the possibility exists that the particles at the interfaces between the weld passes in the PH 13-8 welds, which lead to the ductile secondary cracking along these interfaces, are aluminum oxide and aluminum nitride particles.

Solidification Cracking Susceptibility

Weld solidification cracks may form during the final stages of solidification if sufficient stress or strain occurs to fracture the solidifying structure. Cracking occurs primarily along grain boundaries containing low-melting liquids. The weld solidification cracking susceptibility of Custom 450, PH 13-8 and 15-5 PH was evaluated using sub-size Varestraint testing (Refs. 6, 21). The test results, plotted as total fusion zone crack length vs. augmented strain, are shown in Fig. 19. For comparison, results from two heats of 304L, one that solidified as primary ferrite, 304L-F, with a measured ferrite number FN = 4.5, and the other that solidified as primary austenite, 304L-A with FN~1, are also plotted. The Varestraint test results show that PH 13-8 is extremely resistant to solidification cracking; no cracking occurred at applied strains less than 2%, comparable to that of primary ferrite solidified 304L. Custom 450 and 15-5 PH exhibited similar cracking behavior and were more crack susceptible than PH 13-8. However, the behavior of the two alloys was much closer to the heat

Table 4 — Maximum Crack Length in Varestraint Test (mm)

Alloy	1.5ε	2%ε	3%ε
Ph 13-8 Mo	0	0.18	0.25
Custom 450	0.4	0.50	0.55
15-5 PH	0.30	0.50	0.50

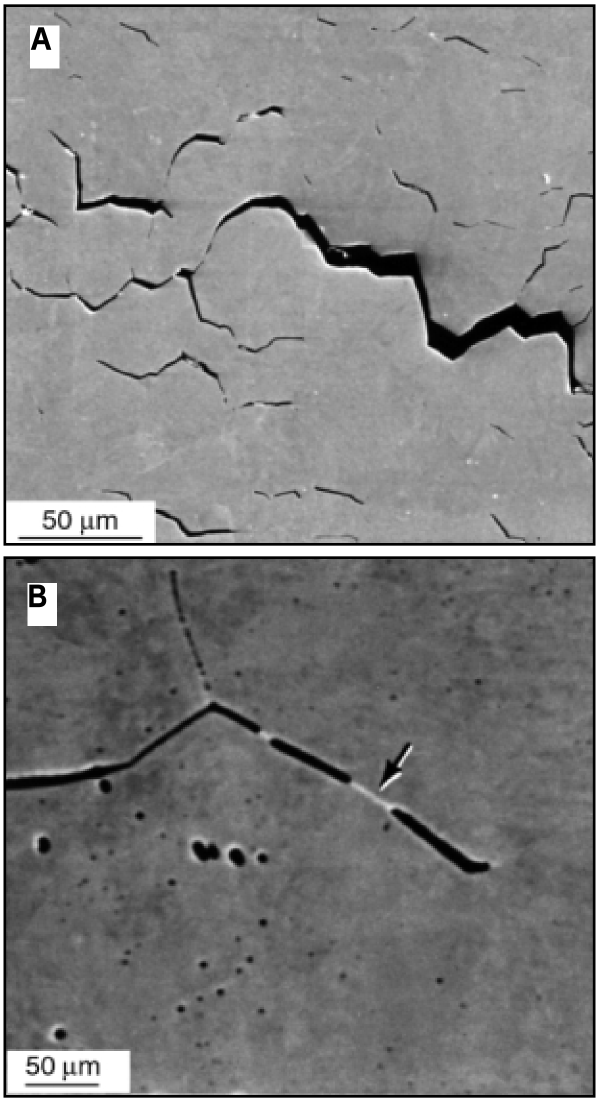

Fig. 21 — A — Shallow intergranular surface cracks in the weld HAZ of a 15-5 PH Varestraint test specimen; B — higher magnification of A showing Cu in the grain boundaries.

304L-F solidifying as primary ferrite than that of primary austenite, 304L-A, especially at the low strain levels. The maximum crack lengths of the martensitic stainless steels for three different strain levels are shown in Table 4. It can be seen the maximum crack length for Custom 450 and 15-5 PH are very similar and are about twice as long as those of PH-13-8 Mo. This behavior is consistent with the total crack length data shown in Fig 19.

Solidification cracks were analyzed to determine the nature of the phases associated with cracking that could be identified at room temperature. Crack tips of a Custom 450 Varestraint sample are shown in Fig. 20A. Little observable microsegregation is evident except in the boundaries in front of the crack. Analytical electron microscopy analysis of particles extracted from the grain boundary regions showed the second phase contained primarily Nb and lighter elements. The electron diffraction patterns index as Nb(C,N). Microprobe analysis of the region containing the second phases also showed enrichments of P.

The crack tip region of a PH 13-8 is shown in Fig. 20B. In these samples, little evidence of microsegregation exists except for a slight segregation a few microns ahead of the crack tip. This region contains higher Ni (~12%) vs. the average alloy composition 8%Ni, and higher Mo, ~5 vs. ~2.2% for the alloy average. The few light second-phase particles in Fig. 20B are high in Mo and P but were not identified. The lacy second phase to the bottom left of the micrograph is delta ferrite residual from the solid-state transformation of ferrite to austenite.

The weld solidification cracks in 15-5 PH were very similar in appearance to those shown in Fig. 20A for Custom 450 and contain the same Nb(C,N) particles. The 15-5 PH Varestraint test specimens also exhibited very small shallow intergranular surface cracks in the weld HAZ. An example of these cracks in a metallographically prepared sample is shown in Fig. 21A. These cracks, shown at higher magnification in Fig. 21B, were associated with Cu apparent as a solidified liquid in the grain boundary (note arrow in Fig. 21B). These surface cracks are attributed to the vaporization of Cu under the arc and its condensation on the cooler base metal ahead of the weld. During Varestraint testing, strains were sufficient at temperatures above the melting point of Cu for the fine surface cracks to form.

Discussion of Solidification Cracking

The extensive use of the austenitic stainless steel alloys and the knowledge of their solidification mode and cracking susceptibility provides a good basis for comparison of the three martensitic alloys. Welds in the 300 series alloys that solidify as austenite can be very susceptible to solidification cracking. The cracking susceptibility increases with increasing levels of P, S and Si that promote the formation of low-melting liquids. However, compositions that solidify as primary ferrite with the peritectic solidification of austenite, or in which the transformation of ferrite to austenite starts to occur at a temperature close to the bulk solidus, are extremely resistant to cracking (Refs. 22–25), even with high levels of P and S (Refs. 26, 27). In compositions that solidify completely as ferrite and the solid-state transformation of ferrite to austenite does not occur until lower temperatures, cracking susceptibility can then again increase (Ref. 28). The results in Fig. 19 for 304L-A and 304L-F are consistent with the known solidification behavior of 304L.

Figure 19 shows like primary ferrite solidified 304L (304L-F), the PH 13-8 was very resistant to solidification cracking. The cracks that did form were fairly blunt in nature, indicating that a high degree of strain was required for their initiation and propagation. One of the reasons for the high cracking resistance is evident when examining regions of the cracks that did form when highly strained. Fig. 20B shows extensive second phases were not associated with the solidification cracks and only a small degree of microsegregation is present. However, it is more informative to examine the solidification front of the tin-quenched welds in Fig. 5A, where the microsegregation and microstructure is characteristic of that when the cracks form. Here, it is more evident that the composition of the liquid present when cracking occurred is enriched in Ni and Mo. Nevertheless, the degree of segregation is still relatively small due to the absence of minor alloying elements, such as Nb with small partitioning coefficients. In this alloy, Si and the impurities, P and S, which further promote low-melting liquids, are also very low. Thus, the absence of reaction products of low-melting liquids in the solidifying microstructure is consistent with the high solidification cracking resistance and relative short crack lengths in the Varestraint tests.

The alloys Custom 450 and 15-5 PH are more crack susceptible than the alloy PH 13-8, even though all three alloys solidified as single-phase ferrite. In these alloys, the examination of Varestraint samples (Fig. 19A) shows the second phases present that can be related to cracking. However, the tin-quenched welds (Fig. 3) further show the high degree of alloy partitioning of a number of elements; the welds also show the degree of microsegregation occurring, which leads to the formation of low-melting liquid. These results would suggest the synergistic effects of a number of elements, though the examination of Varestraint samples may simply suggest the segregation of a Nb-containing liquid solidifying by a eutectic reaction involving NbC. It can also be expected that the elements Si and P may have further suppressed the temperature of final eutectic solidification.

The maximum crack lengths of the Varestraint tests are related to the temperature range of the cracking susceptible region and the thermal gradient in the region in which the crack forms. Since the low-temperature solidification reactions are similar for Custom 450 and 15-5 PH, it is not surprising that the maximum crack lengths of the two alloys are also similar. They are also much greater than those in PH-13-8 Mo, in which no significant secondary solidification reactions were observed.

Summary

The evolution of weld solidification behavior and microstructure development was clearly revealed using tin-quenching techniques. All three alloys were shown to solidify completely as ferrite, even though some existing diagrams predict that PH 13-8 would solidify as primary ferrite with some secondary solidification of austenite. A high degree of alloy partitioning occurs during solidification, but the welds are almost completely homogenized during further solidification and cooling.

The strength and Charpy impact properties of the weld and base metals were qualitatively similar for the aging conditions studied. This similarity in the properties of the base metals and the welds was attributed to homogenization occurring during solidification and cooling, which leads to very similar microstructure and precipitate distribution. However, there were systematic differences between the aging responses of the weld and base metals; in particular, the welds had, at lower aging temperatures, a stronger aging response than did the base metals. In addition, the toughness of the welds exhibited an embrittlement at lower aging temperatures than did the base metal.

Custom 450 and 15-5 PH would appear from Varestraint tests to be fairly resistant to solidification cracking. In these tests, PH 13-8 was shown to be extremely resistant to solidification cracking. The tin-quenched welds revealed the nature of microsegregation and structure characteristic of the state in which solidification cracking occurs. Cracking of both Custom 450 and 15-5 PH was attributed primarily to the segregation of Nb and the formation of a low-melting liquid, resulting in the eutectic solidification involving NbC. Segregation of Si and Mo may further promote cracking susceptibility.

Acknowledgments

The microprobe analysis by P. Hlava and N. Yang, metallography by A. D. Gardia and laboratory support by J. S. Krafcik, all of Sandia National Laboratories, are greatly appreciated. This work was supported by the U. S. Department of Energy under Contract Number DE-AC04-76DP00789.

References

1. Pollard, B. 1993. Selection of wrought precipitation-hardening stainless steels. *ASM Handbook* 6: 482–494.

2. Pickering, F. B. 1963. Iron and Steel Institute, Pub. 114, London, U.K., p. 131.

3. Haudin, J. M., and Montheillet, F. 1978. Study by electron-microscope of hardening precipitation in delta ferrite of a stainless-steel (15%Cr,7%Ni, 2%MO): evidence of R-phase precipitation. *Metallography* 11(4): 391–438.

4. Pickering, F. B. 1978. *The Physical Metallurgy and the Design of Steels*, Applied Science Publishers Ltd., London, U.K., p. 177.

5. Garrison, Jr., W. M., and Brooks, J. A. 1991. The thermal and mechanical stability of austenite in the low carbon martensitic steel PH 13-8. *Mater. Sci. Eng.* A149: 65–72.

6. Campbell, R. D., and Walsh, D. W. 1993. Weldability testing. *ASM Handbook* 6, 603–613.

7. Brooks, J. A., and Baskes, M. I. 1986. Weld microsegregation characterization and modeling. Conference on Trends in Welding Research. *Advances in Welding Science and Technolgoly*, ed. S. A. David, ASM International, Materials Park, Ohio, pp. 93–99.

8. Brooks, J. A., Li, M., Baskes, M. I., and Yang, N. C. Y. 1997. Roles of dendrite tip undercooling and solid state diffusion on weld microsegregation. *Science and Tech of Weld. and Joining* 2(4): 160–166.

9. Olson, D. L. 1985. Prediction of austenitic weld metal microstructure and properties. *Welding Journal* 64(10): 281-s to 295-s.

10. Kotecki, D., and Siewert, T. A. 1992. WRC constitution diagram for stainless-steel weld metals: a modification of the WRC-1988 diagram. *Welding Journal* 71(5): 171-s to 179-s.

11. Cieslak, M. J., Hills, C. R., Hlava, P. F., and David, S. A. 1990. An investigation of the high temperature and solidification microstructures of PH 13-8 Mo stainless steel. *Metall. Trans. A*, 21A: 2465–2475.

12. Massalski, T. B. 1970. *Phase Transformations*, ASM International, Materials Park, Ohio, pp. 433–486.

13. Brooks, J. A., Baskes, M. I., and Greulich, F. A. 1991. Solidification modeling and solid state transformations in high energy density welds. *Metall. Trans. A* 22A: 915–925.

14. Elmer, J. W., Allen, S. M., and Eager, T. W. 1989. Microstructural development during solidification of stainless steel alloys. *Metall. Trans. A* 20A: 2117–2131.

15. Summers, L. T., and Morris, Jr., J. W. 1985. Improvements in the Weldability of a Superconductor Sheath Material, Lawrence Livermore National Laboratory, UCRL-92346.

16. Brooks, J. A. 1991. The role of solidification and microsegregation on weld performance — austenitic vs. martensitic PH stainless steels.*The Metal Science of Joining*, eds. M. Ceislak, J. Perepezko, K. Kang and M. Glicksman, pp. 107–113. TMS, Warrendale, Pa.

17. Hochanadel, P. W., Robino, C. V., Edwards, G. R., and Cieslak, M. J. 1994. Heat treatment of investment cast PH 13-8 Mo stainless steel: Part 1, mechanical properties and microstructure. *Metall. Trans. A* 25: 789–798.

18. Taillard, R., and Pineau, A. 1982. *Mater. Sci. Eng.* 54: 209.

19. Wojcieszynski, A. L. 1993. Particle spacing and grain size effects, Ph.D. thesis, Carnegie-Mellon University, Pittsburgh, Pa.

20. Hale, G. E., and Nutting, J. 1984. *International Metals Reviews* 29: 273–298.

21. Lundin, C. W., Lingenfelter, A. C., Grotke, G. E., and Lessmann, G. G. 1982. The Varestraint test. Welding Research Council Bulletin, No. 280.

22. Thier, H. 1976. *DVS-Ber*. 41:100–104.

23. Brooks, J. A., and Thompson, A. W. 1991. Microstructural development and solidification cracking susceptibility of austenitic stainless steel. *International Materials Review* 36(1): 16–44.

24. Lippold, J. C. 1982. Weld cracking mechanisms in austenitic stainless steels. *Trends in Welding Research in the United States*, ASM Conference Proceedings, ed. S. David, Materials Park, Ohio, pp. 209–241.

25. Kujanpaa, V. P., David, S. A., and White, C. L. 1986. Formation of hot cracks in austenitic stainless steel welds. *Welding Journal* 65(8): 202-s to 212-s.

26. Brooks, J. A., Thompson, A. W., and Williams, J. C. 1984. A fundamental study on the beneficial effects of delta ferrite in reducing weld cracking. *Welding Journal* 63: 71-s to 83-s.

27. Lundin, C. D., Lee, C. H., and Menon, R. 1988. Hot ductility and weldability of free machining austenitic stainless steel. *Welding Journal* 67(6): 119-s to 130-s.

28. Kujanpaa, V., Suutala, N., Takalo, T., and Moisio,T. 1979. Correlation between solidification cracking and microstructure in austenitic and austenitic-ferritic stainless steel welds. *Welding Research International* 9(2): 55–75.